

# DATA-DRIVEN MAGNETOHYDRODYNAMIC MODEL FOR ACTIVE REGION EVOLUTION

S. T. WU,<sup>1,2</sup> A. H. WANG,<sup>1</sup> YANG LIU,<sup>3</sup> AND J. TODD HOEKSEMA<sup>3</sup>

Received 2006 April 27; accepted 2006 July 19

## ABSTRACT

We present a self-consistent, three-dimensional, magnetohydrodynamics model together with time-dependent boundary conditions based on the projected method of characteristics at the source surface (photosphere) to accommodate the observations. The new physics included in this model are differential rotation, meridional flow, effective diffusion, and cyclonic turbulence effects in which the complex magnetic field structure can be generated through the nonlinear interaction between the plasma and magnetic field. This solution, again, is accomplished by including the time-dependent boundary conditions derived from the method of characteristics. This procedure is able to accommodate observations via self-consistent and appropriate data inputs to the boundary. Thus, subphotospheric (i.e., convective zone) effects, through observations, are able to be coupled with the corona. To illustrate this new model, we have employed an observed active region's (NOAA AR 8100) magnetic field measurements from *SOHO* MDI magnetograms to demonstrate the model's capability. Thus, the evolution of three-dimensional magnetic field, velocity field, and energy transport are shown, thereby enabling us to study the physical mechanisms of AR evolution.

*Subject headings:* MHD — Sun: activity — Sun: atmospheric motions — Sun: magnetic fields — Sun: photosphere

*Online material:* color figures

## 1. INTRODUCTION

To improve our understanding of the Sun-Earth connection, it is necessary to acquire knowledge of the Sun's magnetic field and plasma, which drive the corona and heliosphere. Specifically, solar eruptive phenomena are major factors in modulating the solar wind characteristics at the Earth and other locations. Thus, an understanding of the sources of solar eruptive phenomena requires knowledge of the evolution of the active region. By looking at the full disk of photospheric magnetograms, it is obvious that the evolution of sunspots and sunspot groups are the sources of the most powerful solar eruptions (Zirin 1988; Wang et al. 2002, 2004). Modeling the evolution of the active region is still a challenge. In an early study, Leighton (1964) modeled the sunspots and solar cycle in relation to expansion and migration of unipolar magnetic regions (UMRs) and bipolar magnetic regions (BMRs). Since then, a number of investigators (DeVore et al. 1985; McIntosh & Wilson 1985; Sheeley et al. 1985; Sheeley & DeVore 1986; Wilson & McIntosh 1991; Wang & Sheeley 1991; McKay 2003) have extensively investigated the magnetic flux transport in relation to the solar cycle by means of a modified Leighton model. Wang & Sheeley (1991) presented a numerical simulation including differential rotation, supergranular diffusion, and a poleward surface flow (i.e., meridional flow) of the redistribution of magnetic flux erupting in the form of BMRs. They reproduced many of the observed features of the Sun's large-scale field that were not encompassed by Leighton (1964). Wilson & McIntosh (1991) compared the observed evolution of large-scale magnetic fields with the simulated evolution based on the kinematic model of DeVore & Sheeley (1987). They concluded that there must be significant contributions to the evolving patterns by nonrandom flux eruptions within the network

structure, independent of active regions. McKay (2003) presented a magnetic flux transport simulation of the Sun's surface distribution of magnetic fields during Maunder minimum. All these works were focused on the large-scale field and long-timescale (i.e., solar cycle) evolution. Schrijver (2001) has extended the classic Leighton model with ephemeral regions and the early phase of decay of the active region to simulate the dynamic photospheric magnetic field. In another work, Schrijver & Title (2001) demonstrated that the importance of the combination of supergranulation-driven dispersal and meridional advection of the fields leads to a strong polar cap field. Welsch et al. (2004) developed a new technique, i.e., the induction local correlation tracking (ILCT) method, to reveal the velocity field on the photospheric surface by including the magnetic induction equation with the measured magnetic field.

However, all of the above investigations have not invoked full magnetohydrodynamic (MHD) theory, which means that nonlinear dynamic interactions between the plasma flow field and magnetic field are ignored. But, some investigators (Shibata et al. 1989; Matsumoto et al. 1998; Fan 2001) do consider nonlinear interaction of the magnetic field and plasma during the flux emergence without differential rotation and meridional flow. In order to include this nonlinear dynamic interaction, Wu et al. (1993) constructed a quasi-three-dimensional, time-dependent incompressible MHD model with differential rotation, meridional flow, and effective diffusion, as well as cyclonic turbulence, to study the evolution of BMRs. In their limited quasi-three-dimensional theoretical study, they demonstrated that the observed complex magnetic field pattern could arise on the Sun's surface due to the nonlinear interaction between the flow field and magnetic field (i.e., MHD effect) and growth and decay of a BMR. If the MHD effect is ignored, Leighton's diffusion model is recovered.

More recently, Wu et al. (2005) presented a fully three-dimensional, time-dependent, compressible MHD model with differential rotation, meridional flow, effective diffusion due to random motion of granules or supergranules, and the cyclonic turbulence effect to study active region evolution. They successfully deduced nonpotential magnetic field parameters (Falconer

<sup>1</sup> Center for Space Plasma and Aeronomic Research, University of Alabama, Huntsville, AL 35899; wus@cspar.uah.edu.

<sup>2</sup> Department of Mechanical and Aerospace Engineering, University of Alabama, Huntsville, AL 35899.

<sup>3</sup> W. W. Hansen Experimental Physics Laboratory, Stanford University, Stanford, CA 94305-4085.

et al. 2002) for possible initiation of solar eruptive events using an empirical procedure for observational inputs.

In this paper we revisit this problem with direct input of observations on the photospheric boundary to make our new approach a data-driven MHD model. The mathematical model and initial and boundary conditions are presented in § 2. Our numerical results and concluding remarks are given in §§ 3 and 4, respectively.

## 2. MATHEMATICAL MODEL AND INITIAL AND BOUNDARY CONDITIONS

### 2.1. Mathematical Model

The mathematical model appropriate for the physical scenario we have described in the previous section can be expressed by a set of compressible, resistive MHD equations identical to those given by Wu et al. (2005). This set of governing equations consists of conservation of mass, momentum, and energy, and the induction equation resulting from Maxwell's equations. These equations account for the nonlinear dynamic interactions of plasma flow and magnetic field that produce the complex features in the solar atmosphere. For completeness, we repeat these governing equations as follows:

$$\frac{\partial \rho}{\partial t} + \nabla \cdot (\rho \mathbf{u}) = 0; \quad (1)$$

$$\rho \left( \frac{\partial \mathbf{u}}{\partial t} + \mathbf{u} \cdot \nabla \mathbf{u} \right) = -\nabla p + \frac{1}{4\pi} (\nabla \times \mathbf{B}) \times \mathbf{B} + \mathbf{F}_g - 2\rho \boldsymbol{\omega}_0 \times \mathbf{u} - \rho \boldsymbol{\omega}_0 \times (\boldsymbol{\omega}_0 \times \mathbf{r}) + \Psi, \quad (2)$$

where

$$\begin{aligned} \Psi &= -\frac{2}{3} \nabla \cdot (\mu_t \nabla \cdot \mathbf{u}) + \mu_t [\nabla^2 \mathbf{u} + \nabla (\nabla \cdot \mathbf{u})] \\ &\quad + 2[(\nabla \mu_t) \cdot \nabla] \mathbf{u} + [(\nabla \mu_t) \times (\nabla \times \mathbf{u})]; \\ \frac{\partial p}{\partial t} + \mathbf{u} \cdot \nabla p + \gamma p \nabla \cdot \mathbf{u} \\ &= (\gamma - 1) \nabla \cdot \mathbf{Q} + (\gamma - 1) \left[ \eta \mathbf{J}^2 + \frac{\mu}{2} (\nabla \cdot \mathbf{u})^2 \right]; \end{aligned} \quad (3)$$

$$\frac{\partial \mathbf{B}}{\partial t} = \nabla \times (\mathbf{u} \times \mathbf{B}) + \lambda (\nabla \times \mathbf{B}) + \eta \nabla^2 \mathbf{B}. \quad (4)$$

In these equations,  $\rho$  is the plasma mass density,  $\mathbf{u}$  is the plasma flow velocity vector,  $p$  is the plasma thermal pressure,  $\mathbf{B}$  is the magnetic induction vector,  $\mathbf{J}$  is the electric current, and  $\mathbf{Q}$  is the heat conduction. The other quantities are defined as follows:  $\boldsymbol{\omega}_0$  is the angular velocity of solar differential rotation referring to the center of the solar coordinate system given by Snodgrass (1983). The meridional flow profile used here is given by Hathaway (1996).  $\mathbf{F}_g$  is the gravitational force, and  $\gamma$ ,  $\mu$ ,  $\lambda$ , and  $\eta$  are the specific heat ratio (1.05), the viscosity, and the coefficients of cyclonic turbulence and effective diffusion. Finally,  $\Psi$  represents the viscous dissipation.

This set of MHD equations differs from first-principle ideal MHD theory because of the inclusion of additional physics. For example, the additional terms in equation (2) represent the inertial coriolis force (i.e.,  $2\rho \boldsymbol{\omega}_0 \times \mathbf{u}$ ) and the centrifugal force  $[\rho \boldsymbol{\omega}_0 \times (\boldsymbol{\omega}_0 \times \mathbf{r})]$  due to the Sun's differential rotation. The terms  $\eta \nabla^2 \mathbf{B}$  and  $\lambda (\nabla \times \mathbf{B})$  in equation (4) represent the effective diffusion due to random motion of granules or supergranules and the cyclonic turbulence effect, respectively.

### 2.2. Initial and Boundary Conditions

To seek a numerical solution for this mathematical model given in § 2.1, we have cast the set of governing equations in a rectangular coordinate system. The computational domain includes six planes (i.e., four side planes, and top and bottom). The boundary conditions used for the four sides and top plane are nonreflective. In order to accommodate the observation at the bottom boundary, the evolutionary boundary conditions must be used; thus, the method of projected characteristics, originated by Nakagawa (1980, 1981a, 1981b) and implemented by Wu & Wang (1987), is used for the derivation of such boundary conditions. If it is not used, spurious results are likely. The briefly described derivation and its resulting time-dependent boundary conditions are given in the Appendix. In such a way, these boundary conditions are capable of accommodating the observations, which then are able to model the emerging and submerging magnetic flux in a self-consistent way. The numerical technique used for this study is a classical total variation diminishing (TVD) Lax-Friedrichs formulation (Harten 1983; Toth & Odstrčil 1996). To implement this evolutionary simulation of the active region, there are two steps: (1) initialization of the active region model, and (2) simulation of the active region evolution.

#### 2.2.1. Initialization of the Active Region Model

The procedures to initialize the active region MHD model consists of the following steps:

1. Use the observed magnetic field data from the photospheric magnetogram with a potential field model to construct a three-dimensional field configuration. In order to match the chromosphere/corona interface conditions, the magnitude of the field strength is reduced by a factor of 100.

2. Since there are no density measurements on the photosphere, we simply assume that the density distribution at the bottom boundary is directly proportional to the absolute value of the magnitude of the transverse magnetic field and then decreases exponentially with the scale height; thus  $\rho(x, y, z, 0) = [(B_x^2 + B_y^2)/B_0^2]^{1/2} \rho_0 e^{-z/H_g}$ , where  $\rho_0$  and  $B_0$  are constant reference values, which are given with  $H_g$  as the scale height (i.e.,  $H_g = RT_0/g_0$ ,  $g_0$  being the gravitational constant on the surface). In this calculation we have chosen  $T_0 = 10^5$  K,  $R = 1.653 \times 10^{-2}$  km<sup>2</sup> s<sup>-2</sup> K<sup>-1</sup>, and  $g_0 = 0.27$  km s<sup>-2</sup> to give  $H_g$  as  $6.2 \times 10^3$  km. When the magnetic field becomes purely radial (i.e.,  $B_x = B_y = 0$ ), we simply choose the value of the density as the average value of the neighboring four grids. This assumption does bear some physical meaning; that is, usually the observed brighter feature on the surface corresponds with the higher density, which also corresponds with the closed magnetic field. Furthermore, we recognize that the density of the solar atmosphere decreases exponentially with respect to the height in order to maintain hydrostatic equilibrium.

3. We input the results of steps 1 and 2 into the MHD model described in § 2.1 without differential rotation and meridional effects. Because the density is arbitrarily prescribed it makes the pressure gradient not balanced by the gravity force, which induces the velocity by way of the momentum equation. The induced velocity will cause the magnetic field change; thus, the magnetic field is no longer potential. The whole relaxation process begins. Subsequently, the MHD equilibrium state is achieved. This equilibrium state, then, will be the initial state from which we study the active region's evolution. It should be noted that the prescribed pre-initial state is arbitrary. The relaxation of the set of governing equations, in principle, will lead to the MHD equilibrium state. However, the closer the prescribed initial values, the easier it will be to obtain an equilibrium state.

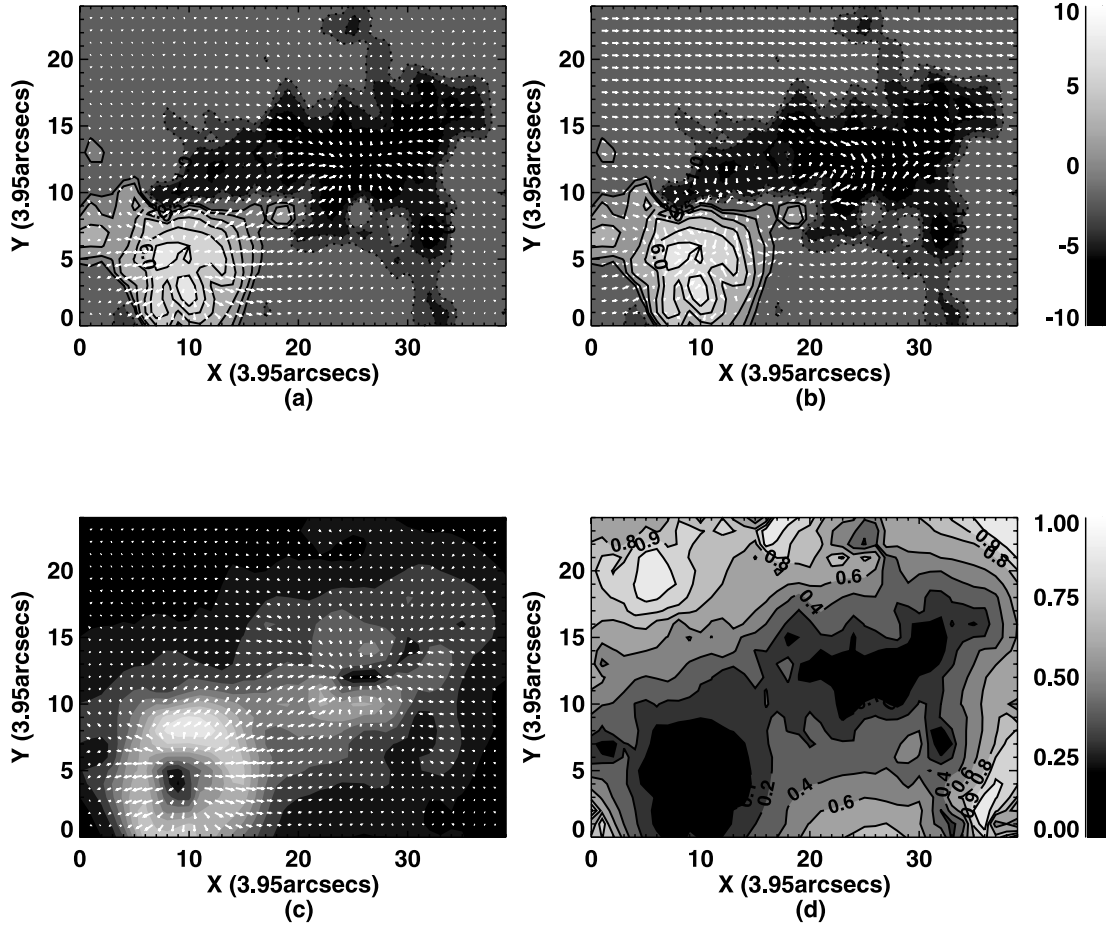


FIG. 1.— Simulated initial state of AR 8100 at 14:27 UT on 1997 October 31. (a) Transverse magnetic field vectors ( $5 \text{ G} \leq |B_r| \leq 6 \text{ G}$ ) and contours of the LOS magnetic field ( $B_z$ ), with the solid and dotted lines representing positive and negative polarity, respectively. The gray-scale bar on the upper right side indicates the strength of the LOS magnetic field ( $-10 \text{ G} \leq B_z \leq 10 \text{ G}$ ) contours. (b) Transverse velocity (maximum is  $1.9 \text{ km s}^{-1}$ ) and  $B_z$  contours. (c) Density contours at the surface with the transverse magnetic field. (d) Plasma beta [ $\beta = (16\pi nkT)/B^2$ ] distribution on the surface. The gray-scale bar on the lower right side is for both density and  $\beta$  contours. [See the electronic edition of the Journal for a color version of this figure.]

### 2.2.2. Simulation of the Active Region Evolution

To evolve the corona on the basis of the evolution of an active region, we input the observed photospheric magnetogram, obtained by the *Solar and Heliospheric Observatory* (SOHO) MDI instrument, in 6 s time steps in accordance with numerical time step constraints. After each step, we allow the corona to respond to the changes in the lower boundary condition. Since the cadence of the MDI measurement is 96 minutes, we have prepared the data by simply taking the difference of the two time sequences of the data and then linearly increasing with time (every 6 s) at the lower boundary with the differential rotation and meridional flow to drive the evolution. The expression used to input the observed magnetogram data is given by

$$B_z(x, y, t) = B_z(x, y, 0) + \sum_{t'} \sum_{n=1}^{960} \Delta B_z(x, y, t') \quad (5)$$

with

$$\Delta B_z(x, y, t') = \frac{B_z(x, y, t' + 1) - B_z(x, y, t')}{960}, \quad (6)$$

where  $t'$  is the time step corresponding to the cadence of the MDI magnetograms. Since the computational time step is 6 s, it takes

960 steps to achieve the cadence of MDI magnetogram measurements. It should be noted that equation (5) will replace one of the compatibility equations (A17).

## 3. SIMULATION RESULTS

In order to illustrate the capability of this new model, we have chosen the observed active region NOAA AR 8100 on 1997 October 31 to compute the initial state, which includes the magnetic field topology, density, and velocity distributions. Following this initial state, we compute its evolutionary state. These results are presented in the following sections.

### 3.1. Initial Magnetohydrodynamic Equilibrium State of NOAA AR 8100

We use the procedures described in § 2.2.1 by inputting the SOHO MDI magnetic field measurements of NOAA AR 8100 at 14:27 UT on 1997 October 31. Since the SOHO MDI field measurements of the active region have a resolution of  $\sim 2''$  with  $198 \times 198$  pixels, in order to assure compatibility of the computational grid with the measurement, the computational domain is set as a rectangular box with  $99 \times 99 \times 99$  grid points in Carrington longitude ( $x$ ), latitude ( $y$ ), and height ( $z$ ), respectively. To match the data with the grids, we have taken a two-point average from the measurements. The measurements are used at the four corners. After we input the data together with the density

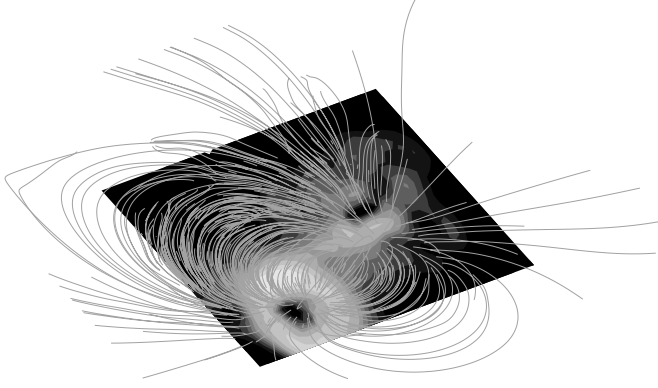


FIG. 2.— Simulated three-dimensional magnetic field configuration of AR 8100 at 14:27 UT on 1997 October 31. [See the electronic edition of the Journal for a color version of this figure.]

distribution, described in § 2.2.1, we allow the numerical model to establish a new equilibrium state via the commonly used numerical time relaxation method. To carry out this procedure, we prescribe a pre-initial arbitrary state as we have discussed in § 2.2.1 into the set of governing equations, in which the system will evolve through a computation loop until an equilibrium state is reached. The criteria of equilibrium is given as  $(f^{n+1} - f^n)/f^n < \epsilon$ , where  $f$  represents all the physical quantities (Hung & Macagno 1966). In this calculation, we have selected  $\epsilon$  to be  $10^{-3}$ . Reaching this equilibrium state takes about 10 Alfvén times.

Physically, this state represents an MHD equilibrium state for NOAA AR 8100 at 14:27 UT, 1997 October 31. Figure 1a shows the contours of the line-of-sight (LOS) component of the magnetic field (the solid and dotted lines represent the positive and negative polarities, respectively) and transverse field vectors at the bottom boundary (i.e., chromosphere/corona interface). Figure 1b shows the transverse velocity vector at the bottom boundary with the same contours of the LOS component of the magnetic field. Figure 1c shows the density distribution where the bright and darker patches represent the high and low intensity of the density with transverse magnetic field vectors, and finally Figure 1d shows the plasma beta  $[\beta = (16\pi nkT)/B^2]$  distributions. Figure 2 shows the corresponding three-dimensional perspective of magnetic field lines and surface density intensity. By viewing these results, we are able to recognize the dynamical physical characteristics of this active region at this particular time. These properties are as follows:

1. The high-density region is at the top of the coronal loops where the stronger transverse magnetic field is concentrated. On the other hand, the core region has low density with most of the field directed radially outward, as shown in Figure 2, and where plasma  $\beta$  is low (Fig. 1d).

2. The transverse velocity at the surface (i.e., chromosphere and coronal interface) exhibits an inflow toward the center, shown as a reverse “Evershed” flow (Athay 1986) at the chromospheric level (Fig. 1b), and a downflow if we view this panel together with Figure 5, which is discussed below.

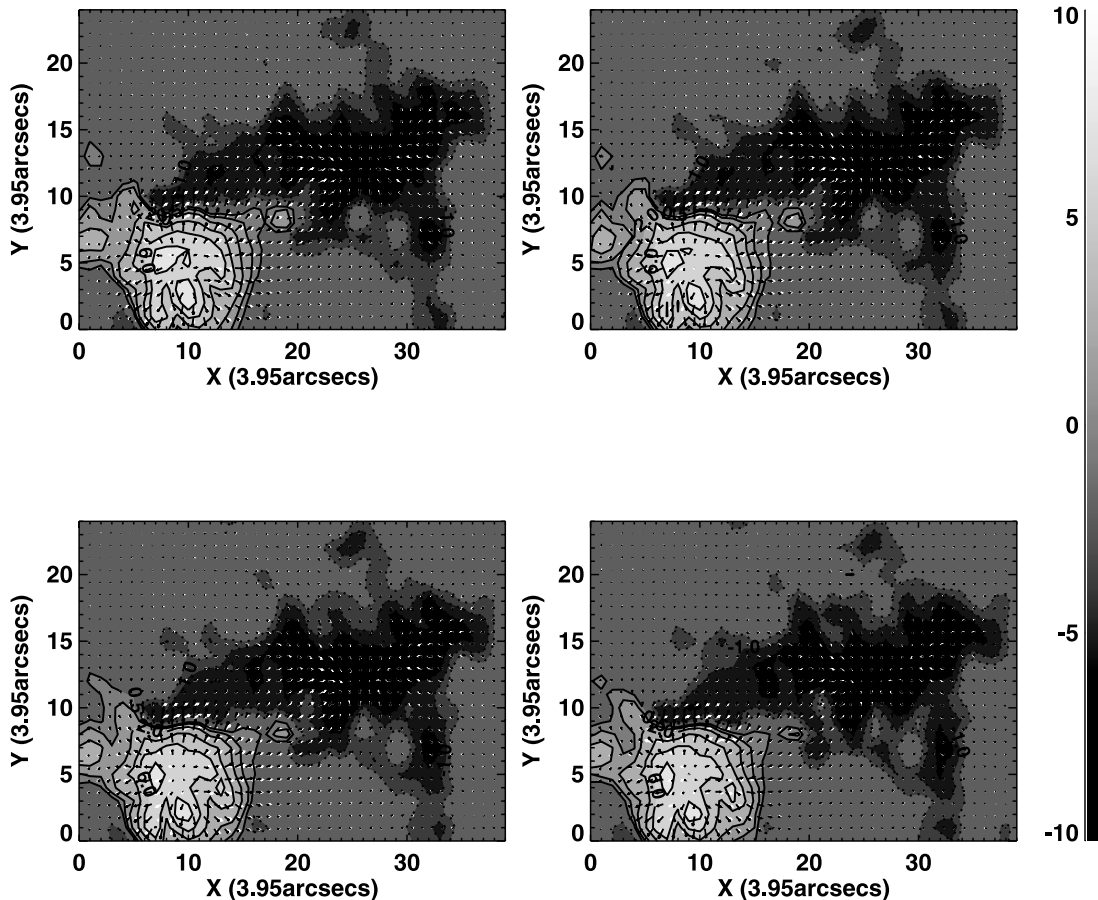


FIG. 3.— Simulated evolution of magnetic field at 14:27 UT (top left), 16:03 UT (top right), 17:39 UT (bottom left), and 19:12 UT (bottom right) on 1997 October 31. The representation is similar to Fig. 1. The gray-scale bar on the right-hand side indicates the strength of LOS magnetic field. The white arrows represent the nonpotential transverse magnetic field, and black arrows represent the potential transverse magnetic field. [See the electronic edition of the Journal for a color version of this figure.]

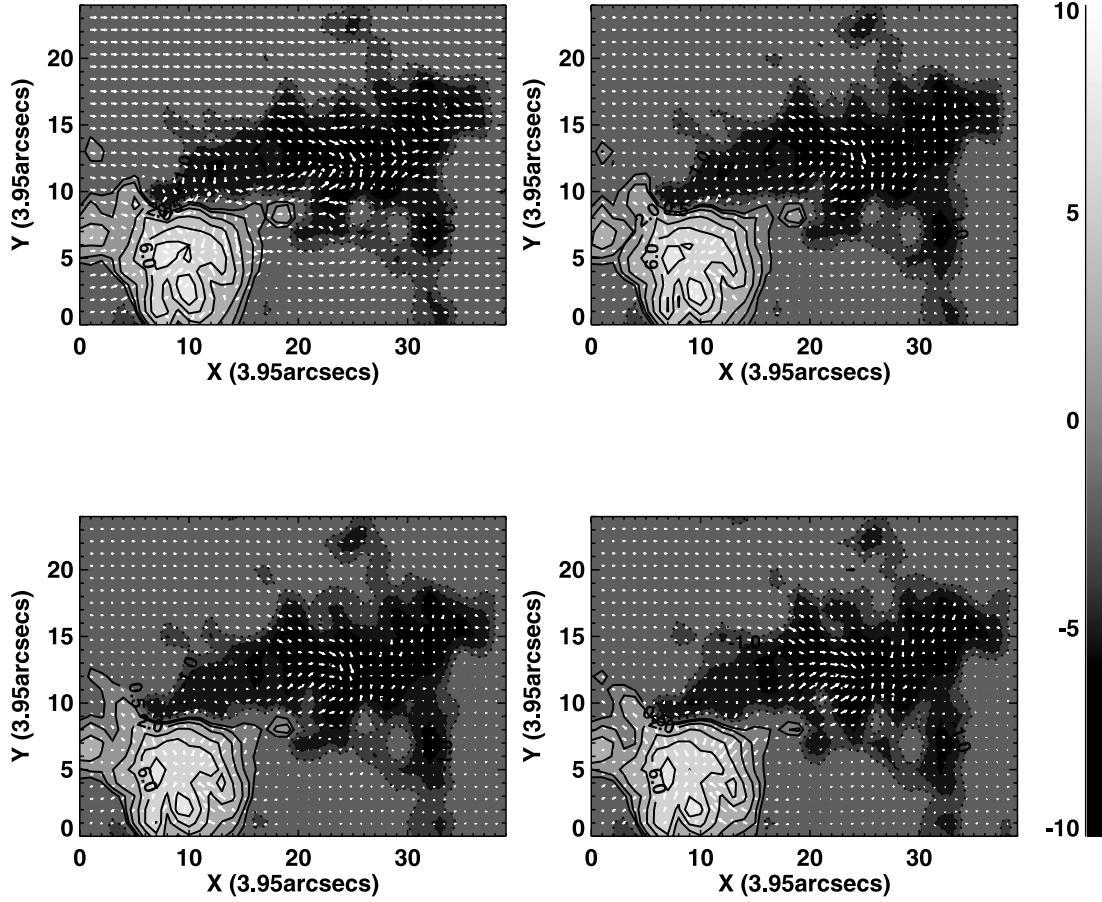


FIG. 4.— Simulated evolution of surface transverse velocity vector ( $V_t$ ), and the contours of the LOS magnetic field for AR 8100 on 1997 October 31 at 14:27 UT with  $0.0002 \text{ km s}^{-1} \leq |V_t| \leq 1.9 \text{ km s}^{-1}$  (top left), 16:03 UT with  $0.0018 \text{ km s}^{-1} \leq |V_t| \leq 3.7 \text{ km s}^{-1}$  (top right), 17:39 UT with  $0.0088 \text{ km s}^{-1} \leq |V_t| \leq 5.0 \text{ km s}^{-1}$  (bottom left), and 19:12 UT with  $0.0164 \text{ km s}^{-1} \leq |V_t| \leq 7.1 \text{ km s}^{-1}$  (bottom right). [See the electronic edition of the *Journal* for a color version of this figure.]

3. The plasma  $\beta$  distribution exhibits chromosphere and corona interface characteristics (i.e.,  $\beta$  is less than 1 everywhere), and the Alfvén speed is inversely proportional to the square root of  $\beta$ . The Alfvén speed values are between  $1.1$  and  $2.5 \times 10^3 \text{ km s}^{-1}$  for this calculation.

### 3.2. Evolutionary State of NOAA AR 8100

Figure 3 shows the nearly 5 hr evolution of transverse magnetic fields and contours of the LOS magnetic field. The gray scale indicates the strength of the magnetic field (light indicates high field strength in the positive-polarity region, and dark indicates high strength in the negative-polarity region; black indicates high strength with negative polarity). The black arrows represent the potential transverse magnetic field, and the white arrows represent the nonpotential (MHD) transverse field. The positive and negative polarities are represented by solid and dotted lines, respectively. By looking at the results, one clearly recognizes that the field is getting stronger and the shear is growing.

Figure 4 shows the corresponding transverse velocity distributions and the contours of the LOS magnetic field. Again, we see the inflow motion toward the center around the dark (negative polarity) and the bright (positive polarity) regions where the field lines are radial. The transverse velocity shows a significant increase as time progresses; during the period of simulation ( $\sim 5$  hr), the lower limit of the transverse velocity has increased from  $0.0002$  to  $0.0164 \text{ km s}^{-1}$ , and the higher limit has increased from  $1.9$  to  $7.1 \text{ km s}^{-1}$ . Figure 5 shows the vertical velocity map

corresponding to Figure 4. The siphon flow is clearly recognized from the stronger positive-polarity field (solid contours; as shown in Fig. 1b) to the rather weaker negative-polarity magnetic field region (dotted contours). The magnitude of vertical velocity is about a few tenths  $\text{km s}^{-1}$ . In a recent study, Ryutova & Shine (2006) found the establishment of arclike flows during the flux emergence based on observations that are similar to those that we have obtained in this MHD simulation.

Figure 6 shows the evolution of the amount of magnetic energy ( $B^2/8\pi$ ) across the bottom boundary at each pixel of the 1 km layer (i.e., chromosphere/corona interface). From these results, we see that there are locations where the magnetic energy is increased and in others decreased; these simulated features represent magnetic flux emergence and submergence (or cancellation) as resulting from data. If we integrate with respect to the active region's area, we obtain a total magnetic energy passing through the boundary on the order of  $10^{32}$  ergs, reaching to  $10^{33}$  ergs at the end of the simulation. The other modes of energy (i.e., thermal, kinetic, and gravitation) are an order of magnitude smaller. Thus, the magnetic energy is, as expected, the dominant source of energy in the active region.

Finally, we examine the energy flux through the lower boundary due to surface flow effect, by using the expression given by Demoulin & Berger (2003) in ergs as follows:

$$\left(\frac{dE}{dt}\right)_s = -\frac{1}{4\pi} \int_s (\mathbf{B}_t \cdot \mathbf{V}_t) B_n dS + \frac{1}{4\pi} \int_s B_t^2 V_n dS, \quad (7)$$

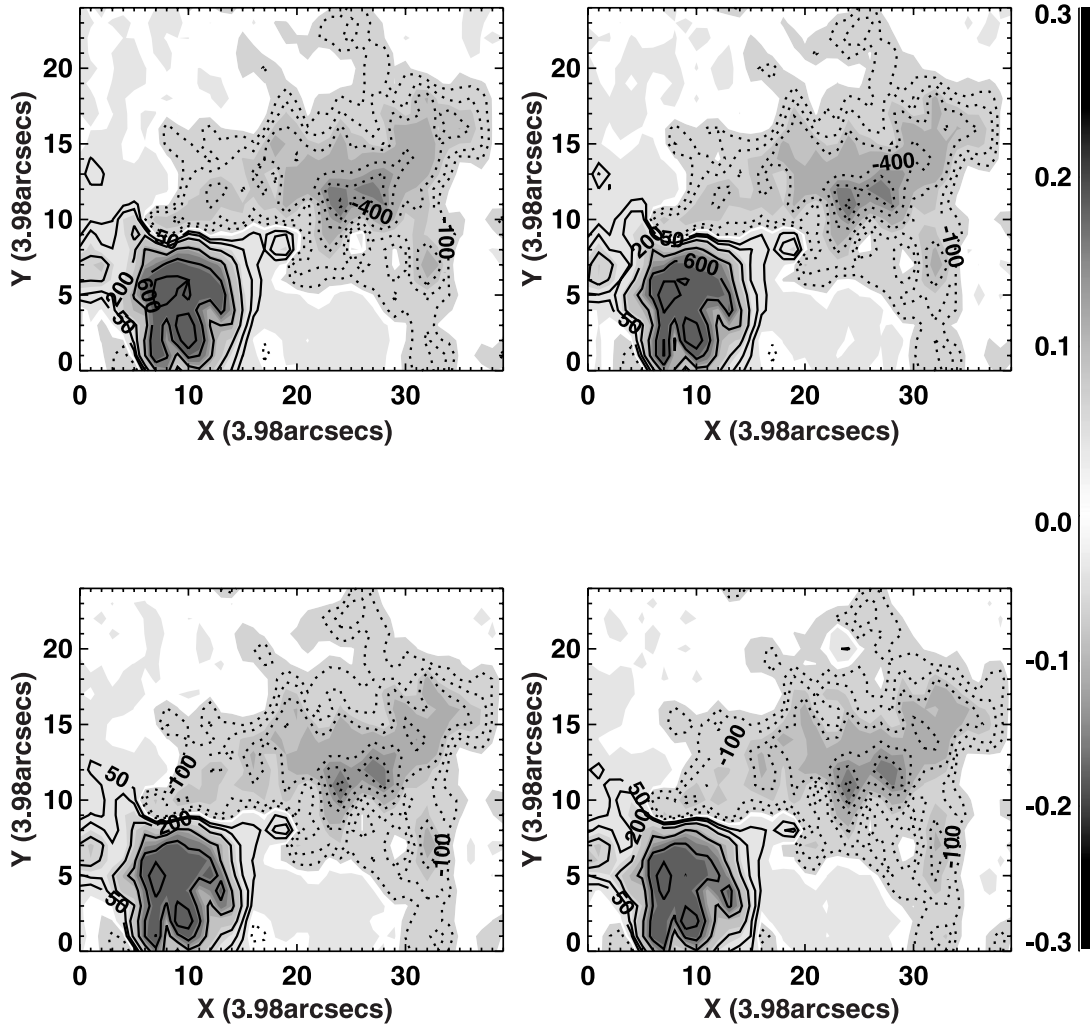


FIG. 5.—Evolution of the vertical velocity ( $\text{km s}^{-1}$ ) of AR 8100 at the same four times on 1997 October 31 as in Fig. 4: 14:27 UT (top left), 16:03 UT (top right), 17:39 UT (bottom left), and 19:12 UT (bottom right). The gray-scale bar on the right-hand side represents the magnitude of the vertical velocity, where the positive-polarity region (solid lines) gives the upward velocity and the negative region (dotted lines) gives downward velocity. [See the electronic edition of the Journal for a color version of this figure.]

where the subscripts  $t$  and  $n$  represent the transverse and normal components of the respective quantity.

Figure 7 shows the energy flux ( $dE/dt$ ), across the lower boundary as a function of the times considered above. It is clearly seen from the above expression that the first term is due to surface flow effect and the second term represents the amount of magnetic flux carried into the active region by the incoming plasma flow, which can be considered to be a direct contribution from emerging and submerging magnetic flux. By examining the results shown in Figure 7, the net magnetic flux emergence is the dominate feature for the growth of the active region at the early stage of about 1 hr. Soon, the term due to the surface flow will take over. This term reflects the importance of the dynamic effect; that is, when the transverse velocity grows, the energy flux term due to the surface flow will also grow. This is consistent with the energy transport by shearing motions found in simulations by Magara & Longcope (2003) and Manchester et al. (2004). Looking at the results shown in Figure 4, the transverse velocity has grown by a factor 82 in the lower limit and a factor of  $\sim 3$  in the higher limit. Thus, energy flux growth due to surface flow is faster than the net magnetic flux emergence. This feature can be understood further; when the magnetic flux emerges from the sub-photospheric surface, the field is not potential and thereby carries

currents; thus, through MHD processes, it induces plasma flow according to a nonlinear procedure described by the magnetic induction equation (i.e., eq. [4]). The induced plasma velocity contributes to the first term of equation (7). Since the velocity grows with the emergence of the magnetic flux, the surface effect represented by the first term overtakes the direct flux emergence. These results are consistent with the analyses based on the observations given by Lites et al. (1995) and Leka et al. (1996). These investigators argued that the plasma flow that drags the field-line-producing shear is not an efficient process in comparison with the emergence of current-carrying magnetic field (i.e., twisted field). This scenario can be explained by the MHD process described here. When the emergence of the magnetic field is potential, the current is zero, such that the Lorentz force in equation (2) is zero. The magnetic shear can only be generated from the effects of differential rotation and meridional flow, as shown by Wu et al. (1993). This process is a very slow process. In this case, the first term of equation (7) is much smaller than the second term. In short, since the magnetic field measurements (i.e., twisted field) are used as an input for the present simulation, our results show that the magnetic shear can be developed in a rather short time via MHD processes. It is also worth noting that recent analytical work and simulations have demonstrated that

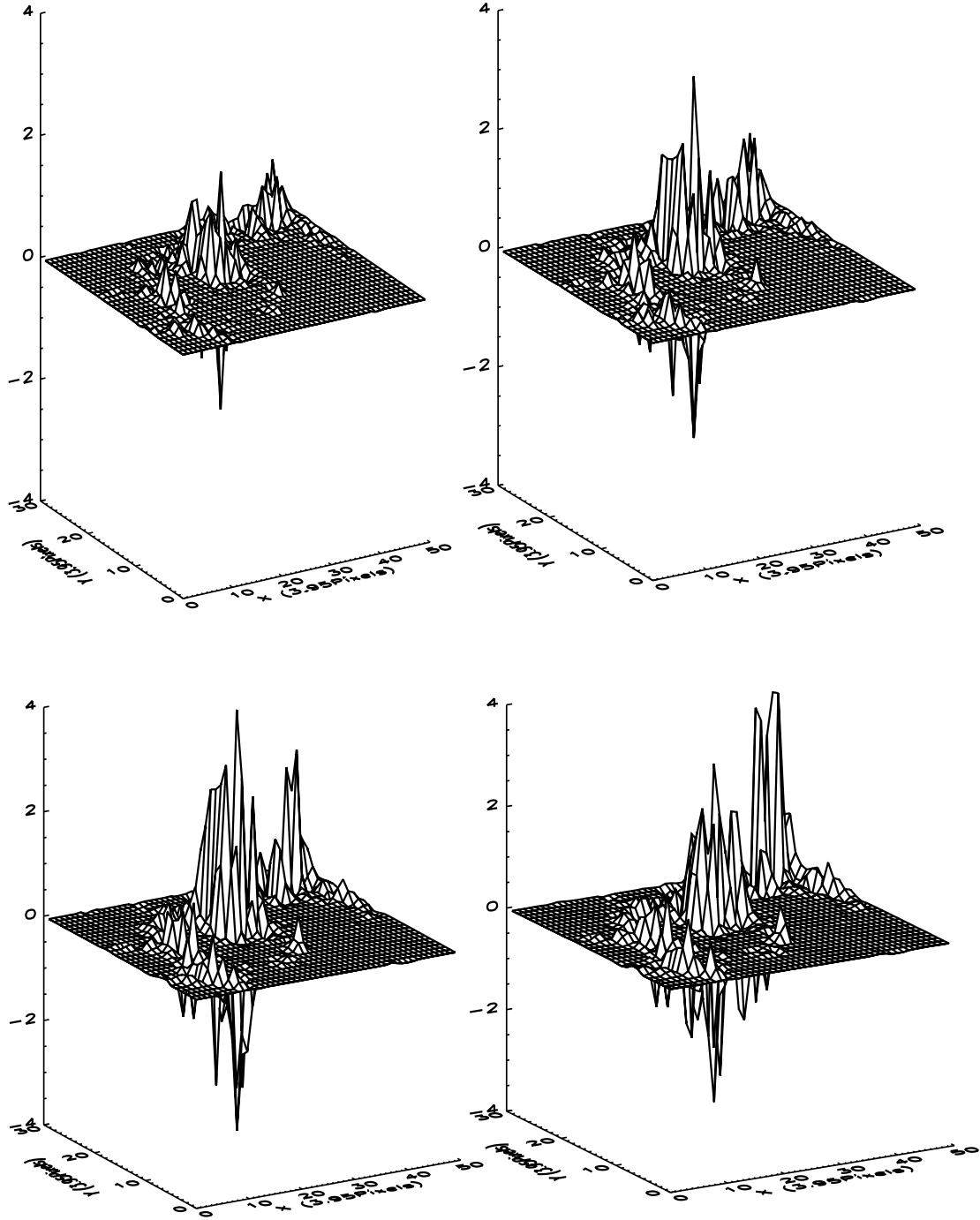


FIG. 6.—Magnetic energy ( $10^{22}$  ergs  $\text{km}^{-2}$ ) across the low boundary to AR 8100 at the same four times on 1997 October 31 as in Fig. 4: 14:27 UT (*top left*), 16:03 UT (*top right*), 17:39 UT (*bottom left*), and 19:12 UT (*bottom right*).

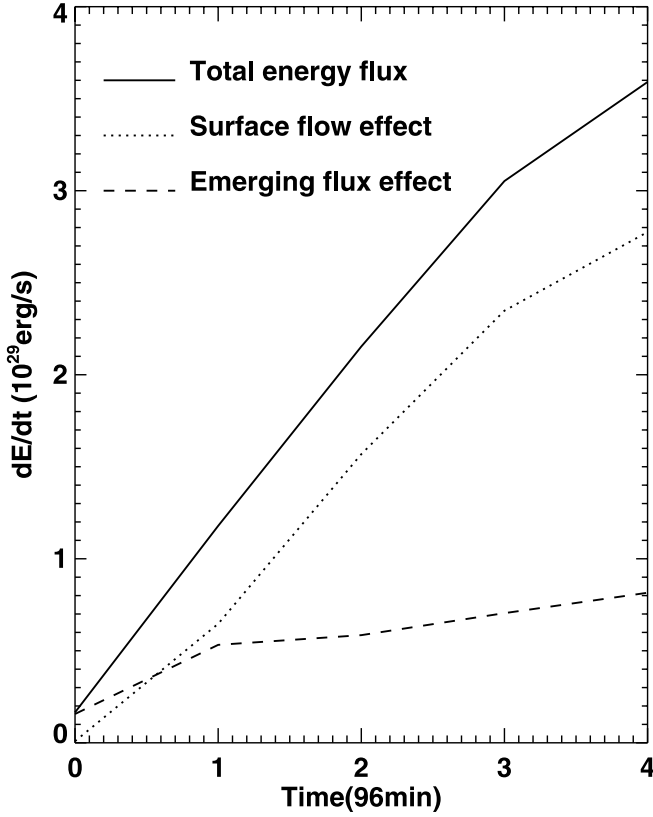


FIG. 7.—Simulated energy flux through the photosphere for AR 8100.

the Lorentz force drives shearing motion during flux emergence (Manchester & Low 2000; Manchester 2001).

#### 4. CONCLUDING REMARKS

In this paper, we have presented a data-driven, three-dimensional, time-dependent, MHD model with differential rotation and meridional flow to investigate an active region's evolution. In order to allow the model to be driven by observations, the time-dependent boundary conditions derived from the method of characteristics are incorporated into the model. Since we use observations to

drive the model self-consistently, the subphotospheric effects are embedded in the measurements. Hence, this model has the capability to couple the photosphere and corona.

To illustrate this model, the example of AR 8100 is presented. We show that the model is able to simulate (1) equilibrium structures and (2) active region evolution on the basis of the observations. We also reveal that the twisted field is the most important factor for the growth of the active region, as shown in Figure 7.

In the present study, some simplifications are made. The plasma properties at the lower boundary are those of a low- $\beta$  plasma; thus, realistic photospheric properties could not be simulated. However, the plasma properties used here are very close to the characteristics at the chromosphere and corona interface (i.e.,  $n_0 = 10^8 \text{ cm}^{-3}$ ,  $T_0 = 10^5 \text{ K}$ ). Recently, Wu et al. (2005) constructed a transition region model to study the propagation of MHD waves; we intend to incorporate this transition region model for the improvement of the current model. Furthermore, the surface velocity distribution has not been directly compared with the ILCT results given by Welsch et al. (2004); however, the present results do show some similarity. In fact, we expect that some differences will occur because of the full MHD features in which the major forces (i.e., Lorentz, pressure, and inertia forces) generate interactions that have great influence on the plasma flow. It should be noted that the ILCT method is based only on the nonresistive magnetic induction equation. Thus, the nonlinear dynamic interaction between the plasma flow and magnetic field of the active region could not be fully recognized in that method. A direct comparison will be made in the future. Finally, it is worth noting that the differential rotation and meridional flow effects are for long-timescale simulations (days, weeks, and more), as demonstrated in our previous work (Wu et al. 1993). The present simulation is driven by the magnetic flux emergence and submergence.

We thank Murray Dryer for reading the manuscript and giving value comments. The work performed by S. T. W. and A. H. W. is supported by NASA grant NAG5-12843, NSF grant ATM 03-16115, and AAMU subcontract under NNG04GD59G. J. T. H. and Y. L. were supported by NASA grant NAG5-13261. *SOHO* is a project of international cooperation between ESA and NASA. Finally, we thank the referee for giving us constructive suggestions.

#### APPENDIX

##### APPLICATION OF THE METHOD OF PROJECTED CHARACTERISTICS FOR THE DERIVATION OF BOTTOM BOUNDARY CONDITIONS

To seek a numerical solution for the mathematical model given in § 2.1, we have cast the set of governing equations in a rectangular coordinate system. The computational domain includes six planes (i.e., four side planes, and top and bottom). The boundary conditions used for the four sides and top boundary are nonreflective. In order to accommodate the observation at the bottom boundary, the evolutionary boundary conditions must be used; thus, the method of projected characteristics originated by Nakagawa (1980, 1981a, 1981b) and implemented by Wu & Wang (1987) are used for the derivation of such boundary conditions.

Using the method of projected characteristics (Nakagawa et al. 1987; Wu & Wang 1987), the bottom boundary conditions are obtained. For a three-dimensional MHD problem, the governing equations are cast in vectorial form,

$$\frac{\partial \mathbf{U}}{\partial t} = -A \frac{\partial \mathbf{U}}{\partial x_1} - B \frac{\partial \mathbf{U}}{\partial x_2} - C \frac{\partial \mathbf{U}}{\partial x_3} + \mathbf{S},$$

where  $\mathbf{U}$  and  $\mathbf{S}$  are column vectors consisting of primary physical quantities such as density, temperature, and the three components of velocity and magnetic field. It should be noted that the differential rotation and meridional flow effects are ignored for the derivation of the boundary conditions. To obtain these characteristics on the boundary, we have chosen the unit normal  $\mathbf{n}$  on the boundary to be along



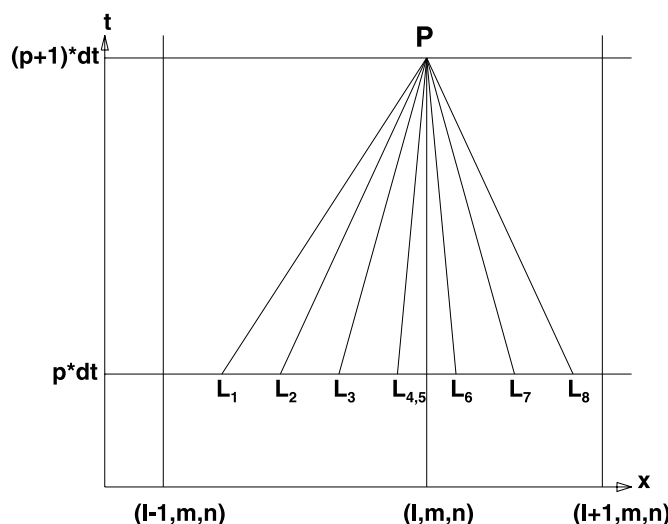


FIG. 8.—Schematic description of the projected characteristics passing the point P at time  $(p + 1)dt$ .

the  $z$ -direction. Thus, the characteristics along the projected normal will be found in the  $z$ - $t$  plane. At the  $z$ - $t$  plane, for a small time difference  $\Delta t$ , the projected characteristics are given by

$$\frac{dz}{dt} = \lambda_i, \quad i = 1, 2, \dots, 8,$$

and can be approximated by straight lines as shown in Figure 8, where  $\lambda_i = (u_z, u_z, u_z + V_A, u_z - V_A, u_z + V_f, u_z - V_f, u_z + V_s, u_z - V_s)$  are eigenvalues. The projected characteristics passing the point P at the time  $(p + 1)\Delta t$  and the spatial location  $(l, m, n)$  then intersect the  $p\Delta t$  axis at  $L_1, L_2, L_3, L_4, L_5, L_6, L_7$ , and  $L_8$ . For  $V_f > V_A > V_s > u_z > 0$ , the projected characteristic  $PL_1$  can be identified with  $\lambda_5 = u_z + V_f$ ,  $PL_2$  with  $\lambda_3 = u_z + V_A$ ,  $PL_3$  with  $\lambda_7 = u_z + V_s$ ,  $PL_{4,5}$  with  $\lambda_{1,2} = u_z$ ,  $PL_6$  with  $\lambda_8 = u_z - V_s$ ,  $PL_7$  with  $\lambda_4 = u_z - V_A$ , and  $PL_8$  with  $\lambda_6 = u_z - V_f$ . With their left eigenvectors, the projected normal characteristic equations (i.e., compatibility equations) are

$$\eta_j \frac{\partial U}{\partial t} + \lambda_j \eta_j \frac{\partial U}{\partial z} = -\eta_j A \frac{\partial U}{\partial x} - \eta_j B \frac{\partial U}{\partial y} + \eta_j S, \quad j = 1, 2, \dots, 8. \quad (A1)$$

They are as follows:

$$dz/dt = u_z$$

$$a^2 \frac{\partial \rho}{\partial t} - \frac{\partial p}{\partial t} = -a^2 \mathbf{u} \cdot \nabla \rho + \mathbf{u} \cdot \nabla p, \quad (A2)$$

$$\frac{\partial B_z}{\partial t} = -\mathbf{u} \cdot \nabla B_z - B_z \left( \frac{\partial u_x}{\partial x} + \frac{\partial u_y}{\partial y} \right) + B_x \frac{\partial u_z}{\partial x} + B_y \frac{\partial u_z}{\partial y}. \quad (A3)$$

$$dz/dt = u_z + V_A$$

$$-B_y B_z \frac{\partial u_x}{\partial t} + B_x B_z \frac{\partial u_y}{\partial t} + B_y V_A \frac{\partial B_x}{\partial t} - B_x V_A \frac{\partial B_y}{\partial t} = A_+. \quad (A4)$$

$$dz/dt = u_z + V_A$$

$$+B_y B_z \frac{\partial u_x}{\partial t} - B_x B_z \frac{\partial u_y}{\partial t} + B_y V_A \frac{\partial B_x}{\partial t} - B_x V_A \frac{\partial B_y}{\partial t} = A_-. \quad (A5)$$

$$dz/dt = u_z + V_f$$

$$-B_x B_z V_f \frac{\partial u_x}{\partial t} - B_y B_z V_f \frac{\partial u_y}{\partial t} + \rho V_f (V_f^2 - V_A^2) \frac{\partial u_z}{\partial t} + (V_f^2 - V_A^2) \frac{\partial p}{\partial t} + B_x V_f^2 \frac{\partial B_x}{\partial t} + B_y V_f^2 \frac{\partial B_y}{\partial t} = B_+. \quad (A6)$$

$$dz/dt = u_z - V_f$$

$$+B_x B_z V_f \frac{\partial u_x}{\partial t} + B_y B_z V_f \frac{\partial u_y}{\partial t} - \rho V_f (V_f^2 - V_A^2) \frac{\partial u_z}{\partial t} + (V_f^2 - V_A^2) \frac{\partial p}{\partial t} + B_x V_f^2 \frac{\partial B_x}{\partial t} + B_y V_f^2 \frac{\partial B_y}{\partial t} = B_-. \quad (A7)$$

$$dz/dt = u_z + V_s$$

$$+ B_x B_z V_s \frac{\partial u_x}{\partial t} + B_y B_z V_s \frac{\partial u_y}{\partial t} - \rho V_s (V_s^2 - V_A^2) \frac{\partial u_z}{\partial t} - (V_s^2 - V_A^2) \frac{\partial p}{\partial t} - B_x V_s^2 \frac{\partial B_x}{\partial t} - B_y V_s^2 \frac{\partial B_y}{\partial t} = C_+. \quad (\text{A8})$$

$$dz/dt = u_z - V_s$$

$$- B_x B_z V_s \frac{\partial u_x}{\partial t} - B_y B_z V_s \frac{\partial u_y}{\partial t} + \rho V_s (V_s^2 - V_A^2) \frac{\partial u_z}{\partial t} - (V_s^2 - V_A^2) \frac{\partial p}{\partial t} - B_x V_s^2 \frac{\partial B_x}{\partial t} - B_y V_s^2 \frac{\partial B_y}{\partial t} = C_-. \quad (\text{A9})$$

For the bottom boundary, if the eigenvalue (i.e., wave speed) is negative, that means the boundary condition will be affected by the computational domain, and we have to use the compatibility equation to determine the physical parameter. The number of compatibility equations that have to use is determined by the number of negative eigenvalues.

As an example, if  $u_z > 0$  and  $|u_z| \leq V_A, V_s, V_f$ , then only  $u_z - V_A, u_z - V_s$ , and  $u_z - V_f$  will be negative. In this case, three out of eight physical parameters have to be determined by three compatibility equations, and five could be specified or solved by using compatibility equations. If relaxing the condition in which  $u_z < 0$  and  $|u_z| \leq V_A, V_s, V_f$ , then  $u_z$  (note that this involves two degenerated eigenvalues),  $u_z - V_A, u_z - V_s$ , and  $u_z - V_f$  could be negative. In this case, five out of eight physical parameters have to be determined by five compatibility equations, and three could be given by using compatibility equations for their solutions. For the first case, the expressions that describe the physical parameters of pressure, density, and the components of velocity and magnetic field vary with time on the boundary and are

$$\frac{\partial p}{\partial t} = \frac{V_s^2 B_- + V_f^2 C_-}{2V_A^2 (V_f^2 - V_s^2)}, \quad (\text{A10})$$

$$\frac{p}{\rho^\gamma} = \text{constant}, \quad (\text{A11})$$

$$\frac{\partial u_x}{\partial t} = \frac{B_y [V_s (V_A^2 - V_s^2) B_- - V_f (V_f^2 - V_A^2) C_-]}{2B_z (B_x^2 + B_y^2) V_s V_f (V_f^2 - V_s^2)} + \frac{B_x A_-}{2B_z (B_x^2 + B_y^2)}, \quad (\text{A12})$$

$$\frac{\partial u_y}{\partial t} = \frac{B_x [V_s (V_A^2 - V_s^2) B_- - V_f (V_f^2 - V_A^2) C_-]}{2B_z (B_x^2 + B_y^2) V_s V_f (V_f^2 - V_s^2)} - \frac{B_y A_-}{2B_z (B_x^2 + B_y^2)}, \quad (\text{A13})$$

$$\frac{\partial u_z}{\partial t} = \frac{-(V_s B_- + V_f C_-)}{2\rho V_s V_f (V_f^2 - V_s^2)}, \quad (\text{A14})$$

$$\frac{\partial B_x}{\partial t} = \frac{B_x [(V_A^2 - V_s^2) B_- - (V_f^2 - V_A^2) C_-]}{2V_A^2 (V_f^2 - V_s^2) (B_x^2 + B_y^2)} + \frac{B_y A_-}{2V_A (B_x^2 + B_y^2)}, \quad (\text{A15})$$

$$\frac{\partial B_y}{\partial t} = \frac{B_y [(V_A^2 - V_s^2) B_- - (V_f^2 - V_A^2) C_-]}{2V_A^2 (V_f^2 - V_s^2) (B_x^2 + B_y^2)} - \frac{B_x A_-}{2V_A (B_x^2 + B_y^2)}, \quad (\text{A16})$$

$$\frac{\partial B_z}{\partial t} = -B_z \frac{\partial u_x}{\partial x} + B_x \frac{\partial u_z}{\partial x} - u_x \frac{\partial B_z}{\partial x} - B_y \frac{\partial u_y}{\partial y} + B_y \frac{\partial u_z}{\partial y} - u_y \frac{\partial B_z}{\partial y}, \quad (\text{A17})$$

where the coefficients  $A_-$ ,  $B_-$ , and  $C_-$  are given as follows:

$$\begin{aligned} A_- = & -(u_z - V_A) \left( B_y B_z \frac{\partial u_x}{\partial z} - B_x B_z \frac{\partial u_y}{\partial z} + B_y V_A \frac{\partial B_x}{\partial z} - B_x V_A \frac{\partial B_y}{\partial z} \right) + (B_x B_y V_A - u_x B_y B_z) \frac{\partial u_x}{\partial x} - (B_x^2 V_A - B_x B_y u_x) \frac{\partial u_y}{\partial x} \\ & - \frac{B_y B_z}{\rho} \frac{\partial p}{\partial x} - \frac{B_z}{\rho} (B_x^2 + B_y^2) \frac{\partial B_y}{\partial x} + B_x V_A u_x \frac{\partial B_y}{\partial x} - u_x B_y V_A \frac{\partial B_x}{\partial x} - \frac{B_y B_z^2}{\rho} \frac{\partial B_z}{\partial x} + (B_y^2 V_A - u_y B_y B_z) \frac{\partial u_x}{\partial y} \\ & - (B_x B_y V_A - B_x B_z u_y) \frac{\partial u_y}{\partial y} + \frac{B_x B_z}{\rho} \frac{\partial p}{\partial y} + \frac{B_z}{\rho} (B_x^2 + B_y^2) \frac{\partial B_x}{\partial y} - u_y B_y V_A \frac{\partial B_x}{\partial y} + u_y B_x V_A \frac{\partial B_y}{\partial y} + \frac{B_x B_z^2}{\rho} \frac{\partial B_z}{\partial y}, \end{aligned} \quad (\text{A18})$$

$$\begin{aligned}
B_- = & - (u_z - V_f) \left[ B_x B_z V_f \frac{\partial u_x}{\partial z} + B_y B_z V_f \frac{\partial u_y}{\partial z} + \rho V_f (V_f^2 - V_A^2) \frac{\partial u_z}{\partial z} + (V_f^2 - V_A^2) \frac{\partial p}{\partial z} + B_x V_f^2 \frac{\partial B_x}{\partial z} + B_y V_f^2 \frac{\partial B_y}{\partial z} \right] \\
& - \left[ B_x B_z V_f u_x + a^2 \rho (V_f^2 - V_A^2) + B_y^2 V_f^2 \right] \frac{\partial u_x}{\partial x} - B_y V_f (u_x B_z + B_x V_f) \frac{\partial u_y}{\partial x} + \rho u_x V_f (V_f^2 - V_A^2) \frac{\partial u_z}{\partial x} \\
& - \left[ \frac{B_x B_z V_f}{\rho} + u_x (V_f^2 - V_A^2) \right] \frac{\partial p}{\partial x} - u_x B_x V_f^2 \frac{\partial B_x}{\partial x} - u_x B_y V_f^2 \frac{\partial B_y}{\partial x} - B_x V_f^3 \frac{\partial B_z}{\partial x} + (B_x B_y V_f^2 - u_y B_x B_z V_f) \frac{\partial u_x}{\partial y} \\
& - \left[ u_y B_y B_z V_f + a^2 \rho (V_f^2 - V_A^2) + B_x^2 V_f^2 \right] \frac{\partial u_y}{\partial y} + \rho V_f (V_f^2 - V_A^2) u_y \frac{\partial u_z}{\partial y} - \left[ \frac{B_y B_z V_f}{\rho} + u_y (V_f^2 - V_A^2) \right] \frac{\partial p}{\partial y} \\
& - u_y B_x V_f^2 \frac{\partial B_x}{\partial y} - u_y B_y V_f^2 \frac{\partial B_y}{\partial y} - B_y V_f^3 \frac{\partial B_z}{\partial y} + \rho g V_f (V_f^2 - V_A^2), \tag{A19}
\end{aligned}$$

$$\begin{aligned}
C_- = & (u_z - V_s) \left[ B_x B_z V_s \frac{\partial u_x}{\partial z} + B_y B_z V_s \frac{\partial u_y}{\partial z} + \rho V_s (V_s^2 - V_A^2) \frac{\partial u_z}{\partial z} + (V_s^2 - V_A^2) \frac{\partial p}{\partial z} + V_s^2 \left( B_x \frac{\partial B_x}{\partial z} + B_y \frac{\partial B_y}{\partial z} \right) \right] \\
& + \left[ a^2 \rho (V_s^2 - V_A^2) + B_y^2 V_s^2 + B_x B_y V_s u_x \right] \frac{\partial u_x}{\partial x} + B_y V_s (u_x B_z + B_x V_s) \frac{\partial u_y}{\partial x} - \rho u_x V_s (V_s^2 - V_A^2) \frac{\partial u_z}{\partial x} \\
& + \left[ u_x (V_s^2 - V_A^2) + \frac{B_x B_z V_s}{\rho} \right] \frac{\partial p}{\partial x} + u_x B_x V_s^2 \frac{\partial B_x}{\partial x} + u_x B_y V_s^2 \frac{\partial B_y}{\partial x} + B_x V_s^3 \frac{\partial B_z}{\partial x} - (B_x B_y V_s^2 - u_y B_x B_z V_s) \frac{\partial u_x}{\partial y} \\
& + \left[ a^2 \rho (V_s^2 - V_A^2) + B_x^2 V_s^2 + u_y B_y B_z V_s \right] \frac{\partial u_y}{\partial y} - \rho V_s (V_s^2 - V_A^2) u_y \frac{\partial u_z}{\partial y} + \left[ \frac{B_y B_z V_s}{\rho} + u_y (V_s^2 - V_A^2) \right] \frac{\partial p}{\partial y} \\
& + u_y B_x V_s^2 \frac{\partial B_x}{\partial y} + u_y B_y V_s^2 \frac{\partial B_y}{\partial y} + B_y V_s^3 \frac{\partial B_z}{\partial y} - \rho g V_s (V_s^2 - V_A^2). \tag{A20}
\end{aligned}$$

The Alfvén speed

$$V_A = \frac{B_z}{\sqrt{4\pi\rho}}.$$

The fast MHD wave speed

$$V_f^2 = \frac{1}{2} \left\{ (a^2 + b^2) + [(a^2 + b^2)^2 - 4a^2 V_A^2]^{1/2} \right\}$$

and the slow MHD wave speed

$$V_s^2 = \frac{1}{2} \left\{ (a^2 + b^2) - [(a^2 + b^2)^2 - 4a^2 V_A^2]^{1/2} \right\},$$

with

$$b = \sqrt{\frac{B_x^2 + B_y^2 + B_z^2}{4\pi\rho}}.$$

The sound speed

$$a = \sqrt{\gamma RT}.$$

#### REFERENCES

- Athay, R. G. 1986, in *Physics of the Sun*, ed. P. A. Sturrock (Dordrecht: Reidel), 64
- Demoulin, P., & Berger, M. A. 2003, *Sol. Phys.*, 215, 203
- DeVore, C. R., & Sheeley, N. R., Jr. 1987, *Sol. Phys.*, 108, 47
- DeVore, C. R., Sheeley, N. R., Jr., Boris, J. G., Young, R. T., & Harvey, K. L. 1985, *Sol. Phys.*, 102, 41
- Falconer, D. A., Moore, R. L., & Gary, A. 2002, *ApJ*, 569, 1016
- Fan, Y. 2001, *ApJ*, 554, L111
- Harten, A. 1983, *J. Comput. Phys.*, 49, 357
- Hathaway, D. H. 1996, *ApJ*, 460, 1027
- Hung, T. K., & Macagno, E. O. 1966, *La Houille Blanche*, 21(4), 391
- Leighton, R. B. 1964, *ApJ*, 140, 1547
- Leka, K. D., Canfield, R. C., McClymont, A. N., & van Driel-Gesztelyi, L. 1996, *ApJ*, 462, 547
- Lites, B. W., Low, B. C., Martinez Pillet, V., Seagraves, P., Skumanich, A., Frank, Z. A., & Shine, R. A. 1995, *ApJ*, 446, 877
- Magara, T., & Longcope, D. W. 2003, *ApJ*, 586, 630
- Manchester, W. 2001, *ApJ*, 547, 503
- Manchester, W., Gombosi, T., DeZeeuw, D., & Fan, Y. 2004, *ApJ*, 610, 588
- Manchester, W., & Low, B. C. 2000, *Phys. Plasmas*, 7, 1263
- Matsumoto, R., Tajima, T., Chou, W., Okubo, A., & Shibata, K. 1998, *ApJ*, 493, L43

- McIntosh, P. S., & Wilson, P. R. 1985, *Sol. Phys.*, 97, 59
- McKay, D. H. 2003, *Sol. Phys.*, 213, 173
- Nakagawa, Y. 1980, *ApJ*, 240, 275
- . 1981a, *ApJ*, 247, 707
- . 1981b, *ApJ*, 247, 719
- Nakagawa, Y., Hu, Y. Q., & Wu, S. T. 1987, *A&A*, 179, 354
- Rytova, M., & Shine, R. J. 2006, *J. Geophys. Res.*, 111, A03101, doi: 10.1029/2005JA011422
- Schrijver, C. R. 2001, *ApJ*, 547, 475
- Schrijver, C. R., & Title, A. M. 2001, *ApJ*, 551, 1099
- Sheeley, N. R., Jr., & DeVore, C. R. 1986, *Sol. Phys.*, 103, 203
- Sheeley, N. R., Jr., DeVore, C. R., & Boris, J. P. 1985, *Sol. Phys.*, 98, 219
- Shibata, K., Tajima, T., Matsumoto, R., Horiuchi, T., Hanawa, T., Rosner, R., & Uchida, Y. 1989, *ApJ*, 338, 471
- Snodgrass, H. R. 1983, *ApJ*, 270, 288
- Toth, G., & Odstrčil, D. 1996, *J. Comput. Phys.*, 128, 82
- Wang, H. M., Qiu, J., Jing, J., Spirock, T. J., Yuchyshyn, Y., Abramenko, V., Ji, H., & Goode, P. R. 2004, *ApJ*, 605, 931
- Wang, H. M., Spirock, T. J., Qiu, J., Ji, H., Yuchyshyn, Y., Moon, Y.-J., Denker, C., & Goode, P. R. 2002, *ApJ*, 576, 497
- Wang, Y. M., & Sheeley, N. R., Jr. 1991, *ApJ*, 375, 761
- Welsch, B. T., Fisher, G. H., & Abbett, W. T. 2004, *ApJ*, 610, 1148
- Wilson, P. R., & McIntosh, P. S. 1991, *Sol. Phys.*, 136, 221
- Wu, S. T., Wang, A. H., & Falconer, D. A. 2005, in *IAU Symp. 226, Coronal and Stellar Mass Ejections*, ed. K. P. Kere, J. X. Wang, & Y. Yan (Cambridge: Cambridge Univ. Press), 291
- Wu, S. T., & Wang, J. R. 1987, *Comput. Methods Appl. Mech. Eng.*, 64, 267
- Wu, S. T., Yin, C. L., McIntosh, P., & Hildner, E. 1993, in *IAU Colloq. 141, The Magnetic and Velocity Fields of Solar Active Regions*, ed. H. Zirin, G. Ai, & H. Wang (ASP Conf. Ser. 46; San Francisco: ASP), 98
- Zirin, H. 1988, *Astrophysics of the Sun* (Cambridge: Cambridge Univ. Press)